J MATER RES TECHNOL. 2020;9(xx):8867–8883

Available online at www.sciencedirect.com

jmr&t
Journal of Materials Research and Technology
www.jmrt.com.br

Original Article

Effect of initial microstructure on the deformation heterogeneities of 316L stainless steels fabricated by selective laser melting processing

Amol B. Kale[a], *Jaiveer Singh*[a,c], *Byung-Kyu Kim*[b], *Dong-Ik Kim*[b], *Shi-Hoon Choi*[a,*]

[a] *Department of Printed Electronics Engineering, Sunchon National University, Suncheon, South Korea*
[b] *Center for Energy Materials Research, Korea Institute of Science and Technology, Seoul, South Korea*
[c] *Department of Mechanical Engineering, Indian Institute of Technology Jodhpur, Karwar, Rajasthan, India*

ARTICLE INFO

Article history:
Received 19 January 2020
Accepted 29 May 2020

Keywords:
316L stainless steel
SLM
EBSD
Microstructure
Deformation

ABSTRACT

The selective laser melting (SLM) is a popular additive manufacturing (AM) technique used for the fabrication of metal parts. In the present study, two 316L stainless steel specimens (SLM-I and SLM-II) with different microstructures were fabricated with different levels of energy density by changing the laser power and scanning speed, which are the main SLM process conditions. The deformation and fracture behavior of miniature SLM specimens under uniaxial tension were experimentally measured via optical microscopy (OM), field emission scanning microscopy (FE-SEM), and an electron back-scattered diffraction (EBSD) technique. In order to analyze the deformation heterogeneities under uniaxial tension, the inverse pole figure (IPF) map, kernel average misorientation (KAM) map, Taylor factor (TF) map, grain boundaries (GBs), Σ3 twin boundaries (TBs), and melt pool boundaries (MPBs) developed in deformed SLM specimens were analyzed at different strain levels. The effect of microstructural factors on the deformation heterogeneities of SLM specimens was explained by the evolution of KAM, GBs, MPBs, and Σ3 TBs. The initial microstructures of the SLM specimens significantly influenced the generation and propagation of cracks under uniaxial tension.

1. Introduction

Alloys of 316L austenitic stainless steel (SS) are in high demand in several industries due to their corrosion resistance and high mechanical strength, as well as to superior characteristics of formability and weldability [1,2]. Therefore, these are used in the petrochemical industry [3], the medical sector [4,5], and the nuclear industry [6]. In recent years the mechanical properties of 316L SS have been improved via the extensive optimization of thermo-mechanical processing conditions [7,8]. The well-known manufacturing techniques of 316L SS consist mainly of casting, forging, and extrusion. These techniques have limited degrees of freedom, and their use in the manufacturing of metal parts with complex shape geometries requires post-processing such as machining, which is accompanied by a considerable waste of materials and time.

* *Corresponding author.*
E-mail: shihoon@scnu.ac.kr (S. Choi).
https://doi.org/10.1016/j.jmrt.2020.06.015

The most effective additive manufacturing (AM) technique for the fabrication of 316L SS parts is selective laser melting (SLM) due to excellent advantages that include high process flexibility, high material utilization, a short production time, and excellent corrosion resistance [9]. The SLM process is a rapid prototyping technique that uses metallic powders as a material source [10–12]. The SLM process can directly fabricate complex metal parts via the use of 3-D computer-aided design (CAD) data by selectively melting successive layers of metal powders [10,13]. In the SLM process, a high-energy source is used to fabricate the material. The fabrication of dense metal parts without post-processes such as infiltration, sintering, or aging, coupled with high degrees of individuality and geometric freedom, is considered to be a significant advantage of this process [14,15]. Recently, materials fabricated via the SLM process have been widely used in several industrial applications in the aerospace industry, for medical implantations [16,17], in nuclear reactors [18], in conformal cooling channels [19], and the automobile [20] and rail industries [21]. Many studies have examined the SLM process using various metallic alloys such as tool steels [22], nickel alloys [23,24], NiTi alloys [25,26], Ti alloys, cobalt-based alloys [23,27], and aluminum alloys [28]. In recent research, the SLM process has been used not only to fabricate a single material but also to produce nanocomposite materials. AlMangour et al. [29–31] used the SLM process to improve the mechanical properties of 316L SS with the addition of TiC and TiB_2 nanocomposite materials. Suryawanshi et al. [32] reported significant increases in the yield strength of SLM 316L SS by optimizing the processing conditions.

SLM parts contain various types of heterogeneities, including internal voids, partially melted the powder, internal cracks, variations in chemical composition, and thermal stress, as reported by various authors [33–35]. For manufacturing fully densified and relatively homogeneous metal parts using the SLM process, however, it is necessary to obtain the optimal process parameters. Huang [36] have examined the effects of processing parameters on microstructure and density of 316L SS fabricated by SLM. They reported that the densification was enhanced by increasing the energy density until it arrived at an optimum value, after which the densification rate started to decrease. Choong et al. [37] found out an optimum energy density for achieving the high density and low surface roughness. Simmons et al. [38] revealed an optimum scanning speed for the fabrication of 316L SS by SLM to reduce the porosity caused by partial fusion. Li et al. [39] reported that the densification of 316L SS powder is strongly related to the process parameters of SLM, such as laser power, scanning speed, hatch spacing, thinner layer thickness, and atomization techniques. Yusuf et al. [40] studied the porosity and microhardness of SLM-built 316L SS parts, and the results indicated that the average microhardness values of SLM-fabricated parts were higher than those for wrought manufactured counterparts. The mechanical properties of 316L SS fabricated SLM specimens were influenced by many factors such as powder size, specimen build orientation, scanning strategy, scanning speed, laser power, and hatch distance [41–44,32,45–48]. Chen et al. [41] investigated that the SLM specimens fabricated from the fine powder showed superior mechanical properties. The horizontal fabricated specimen has better mechanical properties than the vertical fabricated specimen examined by Casati and Bahl [44,49]. Sun et al. [50] clarified that the evolution of crystallographic texture from <100>|| BD to <110>|| BD enhances the work hardening rate caused by extensive twining, thereby increasing the strength and ductility of 316L specimen. Prashanth et al. [51] have determined that texture can be controlled either by changing the angle between the specimen and the substrate plate or by post-fabrication isothermal annealing. Suryawanshi et al. [32] revealed that single melt scanning strategies exhibited better mechanical properties than chess scanning strategies, without being affected by higher porosity. Hao et al. [52] established optimum processing conditions for SLM to improve the density and mechanical properties of 316L SS and hydroxyapatite (HA) composites. Miranda et al. [53] used statistical analysis to evaluate the influence that the processing parameters (laser power, scanning speed, and scanning spacing) of SLM exert on the density, hardness, and shear strength of 316L SS. Liverani et al. [42,54] and Kurzynowski et al. [42,54] studied the correlation between the processing parameters, microstructure, and mechanical properties of 316L SS samples fabricated by SLM. Zhang et al. [55] investigated the influence that the processing parameters, environmental conditions, and preheating treatment exert on the mechanical properties of 316L SS fabricated via the SLM process. Yasa and Kruth et al. [11] investigated how re-melting affects the density and the surface roughness of SLM-built 316L SS parts. The deformation behavior of 316L SS micro lattice structures fabricated via the SLM process was investigated in combination with uniaxial loading in an experiment that used an image-analysis technique [56,57]. Riemer et al. [58,59] and Zhang et al. [58,59] investigated the fatigue behavior (crack initiation and crack growth) in 316L SS fabricated via the SLM process. Spierings et al. [60] investigated the effects that different types of surface finishing can exert on the fatigue behavior of 316L SS. The fatigue life of polished specimens was improved compared with that of the as-fabricated material, but lifetime behavior at higher stress amplitudes was not significantly altered for either sample. Wang et al. [61] used a hierarchical technique to understand the relationship of the microstructure-mechanical properties in additive-manufactured 316L SS with high strength and ductility.

Most of the research related to the manufacturing of 316L SS via conventional SLM processing has focused on optimizing the process conditions for improving the mechanical properties [45,53,54,62]. To improve the mechanical properties of the 316L SS fabricated by the SLM process, it is necessary to understand the microstructural effects on the heterogeneity of deformation and fracture, which is different from that of the specimens fabricated via conventional thermo-mechanical processes. However, few studies have been focused on the effect of microstructure on the mechanical properties of 316L SS fabricated by SLM [46,63]. The authors had difficulty locating a detailed study of the effect that the initial microstructures exert on the heterogeneous deformation and fracture behavior of 316L SS specimens fabricated via the SLM process. The objective of the present research was to investigate the effect that the initial microstructure exerts on the

deformation and fracture behavior of 316L SS fabricated via the SLM process under uniaxial tension. For this purpose, two 316L SS specimens with different initial pore densities were prepared for uniaxial tensile tests on the miniature specimen. In order to understand the effect of microstructural factors such as initial pores, melt-pool boundaries (MPBs), grain boundaries (GBs), Σ3 twin boundaries (TBs), and the cellular structure of the deformation heterogeneities of 316L SS fabricated via the SLM process, post-mortem techniques were used for as-fabricated specimens under various strain levels.

2. Experimental details

2.1. *Selective laser melting (SLM)*

In the present study, 316L SS powder (CL20ES, Concept Laser GmbH, Germany) was used as a starting material. The chemical composition of the powder is shown in Table 1. The morphologies of the powders were analyzed via field emission scanning electron microscopy (FE-SEM) using a JEOL (JSM-7100F). A laser diffraction method CILAS 1090 (Cilas, France) was used to measure the particle size distribution after dispersion in water. Fig. 1(a) shows the distribution of powder size and its cumulative value. The particle size analysis of the collected data indicated the following distribution: D10 = 20.68 μm, D50 = 28.62 μm, and D90 = 29.46 μm. Here D10, D50, and D90 correspond to the values of the particle diameter at 10, 50 and 90% in the cumulative value, respectively. D50 is also called as the median diameter. The SLM process was conducted using a concept laser M2 machine. Fig. 1(b) features a schematic diagram that illustrates how the SLM process was conducted inside an M2 machine equipped with a fiber laser with a power of 400 W and a focus diameter of 0.1 mm. The powders of 316L SS were delivered through a powder feeding apparatus, which used a moving roller to create a powder layer. All processing was conducted in a chamber protected by an argon atmosphere with less than 0.2% O_2. The SLM process was performed using two different conditions (SLM-I and SLM-II) in terms of laser power (P) and scan speed (v) to produce a fixed hatch spacing (h) of 100 μm and a layer thickness (d) of 30 μm by using a 50 μm laser beam. The processing parameters for the SLM-I specimen included a laser power of 200 W and a scanning speed of 800 mm/s. A laser power of 300 W and a scanning speed of 1500 mm/s were employed for the SLM-II

Table 1 – The chemical compositions of the powder (wt % except for oxygen).

Elements	C	Cr	Ni	Mo	Mn	Si	P	S	Fe	O
CL20ES	0.06	16.10	10.34	2.62	0.80	0.25	<0.0003	0.03	Bal.	351 ppm

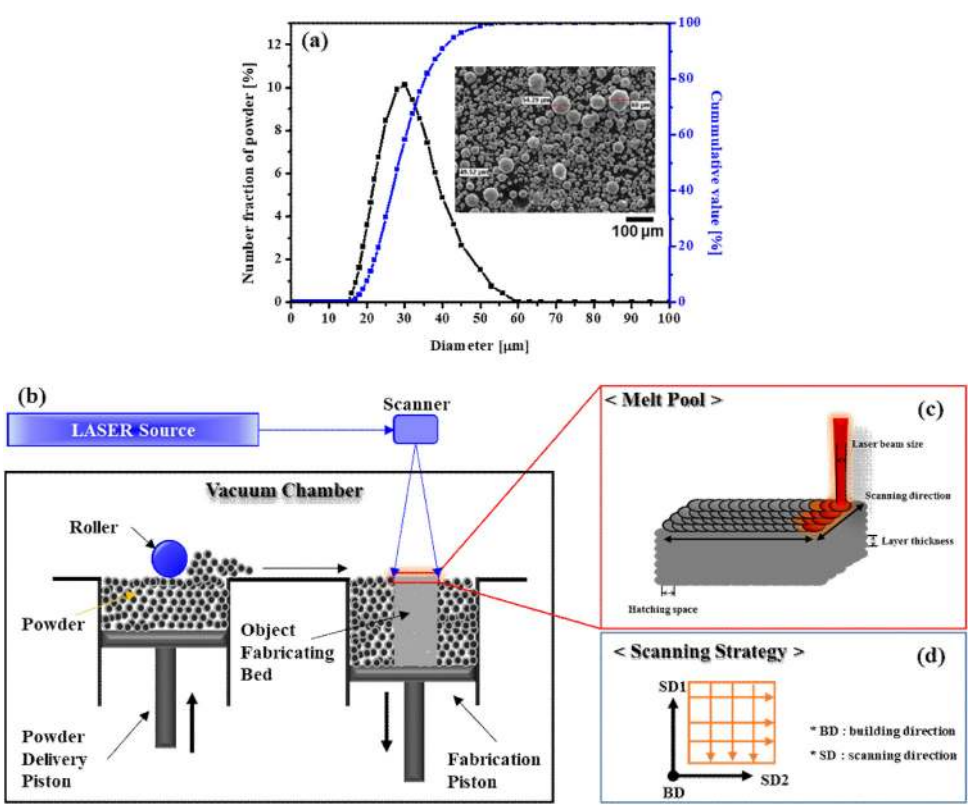

Fig. 1 – (a) FE-SEM image of as-received commercial 316L SS powder, and corresponding powder size distribution, (b) schematic of the SLM apparatus, (c) schematic for the creation of a melt pool, and (d) scanning strategy for the SLM specimens.

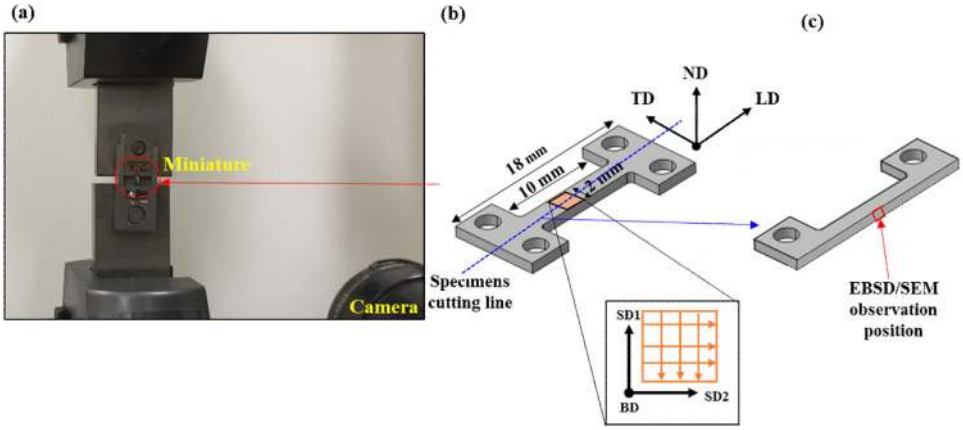

Fig. 2 – (a) Jigs for tensile testing (b) schematic diagram of a miniature specimen (c) EBSD/SEM observation position (marked by a red box) after cutting specimens.

specimen. The energy density, E [J/mm^3], was calculated using the following Eq. (1) [26,64]:

$$E = \frac{P}{v \cdot h \cdot t} \tag{1}$$

where P is the laser power (W), v is the scanning speed (mm/s), h is the hatch spacing (mm), and t is the layer thickness (mm). The SLM-I and SLM-II specimens were fabricated with energy density values of 83.34 and 66.67 J/mm^3, respectively. The amount of energy density is regulated by the power input and the scan speed. Several literatures have researched upon the laser power and scan speed optimization and have presented the range (150–300 W and 700–2200 mm/s) for quality microstructure and mechanical properties. Yakout et al. [35,65] recommended two threshold values for selecting energy density: brittle-ductile transition energy density and critical laser energy density. Below the brittle-ductile transition energy density, the parts revealed void formation, low density, and brittle fracture. Above the critical energy density, the parts showed vaporization of some alloying elements that have a low melting point. As per their suggestion, the energy density should not surpass the critical energy density value. They found stable melting ranges to occur between these two laser energy densities: 62.5–104.2 J/mm^3 for stainless steel 316L. Fig. 1(c) schematically shows how the laser scanning was conducted. The present study used a unidirectional cross-hatched method as a scanning strategy, as shown in Fig. 1(d). Three orthogonal coordinate system, namely building direction (BD), in the first (SD1) and second scanning directions (SD2), were set based on the scanning direction in the SLM process. The density of the specimens was measured using Archimede's method (RADWAG-AS-R-series) [66]. Three samples for each condition were used to obtain the average density of SLM specimens. The average densities of the SLM-I and SLM-II specimens were 7.95 g/cc (99.57%) and 7.55 g/cc (94.57%), respectively, with a standard deviation of 0.0038 and 0.0173.

2.2. *Tensile testing and microstructure characterization*

Tensile tests were conducted using an electronic universal testing machine (Exceed, E44 MTS, USA), as shown in Fig. 2(a). Miniature tensile specimens with a total length of 18 mm, a width of 2 mm, and a thickness of 1.5 mm were fabricated via the SLM process directly. The miniature specimen is not yet standardized but widely used in several literature [67–71] where it is impossible to use standard specimens due to the limited size of the material produced. An important consideration in the design of miniature specimens is to keep the ratio of gauge length and width similar to ASTM standard and subsize specimens (5:1 and 4.17:1). In this study, we followed the 5:1 ratio according to the ASTM E8 standard. Prior to the tensile test, mechanical polishing was performed using SiC paper for the purpose of removing the roughness of the surface of the tensile specimen. A schematic diagram of the miniature tensile specimens is shown in Fig. 2(b) along with the reference sample coordinates: loading direction (LD), transverse direction (TD), and normal direction (ND). The relationship between the coordinate system of the SLM process based on the scanning direction and the coordinate system of the tensile specimens is as follows: LD//SD2, TD//SD1, ND//BD. The digital image correlation (DIC) technique was used to measure the stress–strain curve and strain distribution of SLM specimens under the uniaxial tension testing [71]. The DIC technique is based on the calculation of the strain distribution by measuring the displacement of the speckles scattered on the surface of the tensile specimen [72,73].

Microstructural observation of the as-fabricated SLM specimens was carried out on the center of the transverse direction (TD) section of a tensile specimen. SLM specimens were mechanically polished using SiC paper and colloidal silica. The polished specimens were cleaned ultrasonically with ethanol and then dried under hot air flow, followed by chemical etching using Marble's reagent (10 g $CuSO_4$, 50 ml HCl and 50 ml distilled water) for 50–60 sec. Microstructures were observed using an optical microscope (OM: OLYMPUS GX-51). The microtexture of the as-fabricated SLM specimens was examined

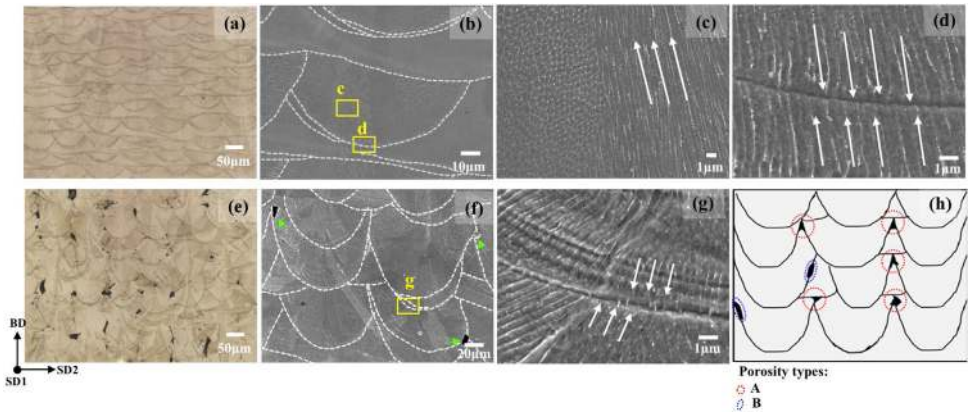

Fig. 3 – Microstructures of as-fabricated SLM specimens analyzed using OM and FE-SEM: (a–d) SLM-I and (e–g) SLM-II, (h) a schematic view of the pore types in the SLM-II specimens.

using electron backscatter diffraction (EBSD) fitted to FE-SEM. The mechanical polishing was conducted using a 1 μm diamond paste for the intermediate stage. Finally, the specimens were polished using 0.04 μm colloidal silica. EBSD analysis was examined by selecting a 400 × 400 μm^2 scanning area at a step size of 0.5 μm. Microtexture examination was performed using TSL-OIM^{TM} (TexSEM Laboratories orientation imaging microscopy) software along with techniques developed specifically for analyzing GBs, Σ3 TBs, image quality (IQ), inverse pole figure (IPF), kernel average misorientation (KAM), and Taylor factor (TF). The KAM is defined as the average misorientation between each measurement point and the nearest neighbors. The 3rd nearest neighbor was used to calculate the KAM at a specific measurement point, and misorientations exceeding a critical value of 5° were excluded in the calculation. In this study, the deformation heterogeneities of SLM specimens was evaluated by the spatial distribution of KAM values.

SLM specimens deformed to different engineering strains were prepared to observe the microstructural changes under uniaxial tension: $e = 0.15$, $e = 0.20$, $e = 0.25$ and e_f for SLM-I specimens, and $e = 0.05$, $e = 0.10$, $e = 0.15$ and e_f for SLM-II specimens, respectively. The deformation behavior of the SLM specimens under different strain levels was experimentally analyzed at the center of the TD section via FE-SEM and EBSD, as shown in Fig. 2(c). The deformed specimens were polished under the same conditions as the as-fabricated specimen mentioned above. EBSD analysis was examined by selecting a 300 × 300 μm^2 scanning area at a step size of 0.5 μm. Additional analyses of the fracture surfaces of the fractured tensile specimens were conducted on the LD section.

3. Results

3.1. *Microstructure characterization*

Microstructures of the as-fabricated SLM specimens analyzed using OM and FE-SEM appear in Fig. 3. In the SLM process, the microstructure of SLM specimens depends on processing parameters such as initial powder size, laser power, scanning speed, scanning strategy, the thickness of the powder layer, and the size of the focusing laser beam [55]. Fig. 3(a) and (b) correspond to the analysis results of the SLM-I measured by OM and FE-SEM, respectively. MPBs were drawn on the SEM image for easy comparison of the microstructural changes according to the SLM process conditions. The solidified scan tracks of the SLM-I specimen were well-arranged parallel to the SD, and the MPBs between the scan tracks were well connected, as shown in Fig. 3(a) and (b). The size of the melt pools depends on processing parameters such as exposure time, input power, and beam size [49]. Wu et al. [74] studied the effect that laser power exerts on the melt pool in 316L SS fabricated by SLM. Fig. 3(c) shows a fine cellular structure, indicated by white arrows, occupying the melt pool. This morphology is due to the high cooling rate of rapid solidification during the SLM process. High-temperature gradients, high and local cooling rate, and directional solidification in laser melting result in cellular and columnar sub-grains existed in the same molten pool. Yasa and Kruth [11] observed a similar cellular structure in 316L SS fabricated by SLM. The overlapped nature of the melt pools is related to the fusion of each layer, as shown in Fig. 3(d). The orientation of the elongated intragranular cells was similar across the MPBs, as indicated by the white arrows in Fig. 3(d). Fig. 3(e) and (f) correspond to the analysis results of the SLM-II specimen, as measured via OM and FE-SEM, respectively. The pores of the SLM-II specimen were relatively non-uniformly distributed on the surface. The results of Fig. 3(e) were obtained by analyzing the locations where several pores were clustered in a particular region. In this paper, the regions where pores were clustered were intentionally selected for analysis of deformation and fracture behavior under uniaxial tension. Fig. 3(g) shows a fine cellular structure, indicated by white arrows, occupying MPBs in Fig. 3(f). Pores with a size of about 9–15 μm were unevenly distributed throughout the SLM-II specimen, as shown in Fig. 3(e). Pores were located at the triple-junction points of the MPBs (indicated by Type A) and at track-track MPBs (indicated by Type B), as explained schematically in Fig. 3(h). Fig. 3(e) shows that the shape of Type A pores exhibited low aspect ratio, while the shape of Type B pores exhibited a high aspect ratio. According to a manual observation of the microstructure, the number of Type A pores was relatively larger than the number of Type B pores.

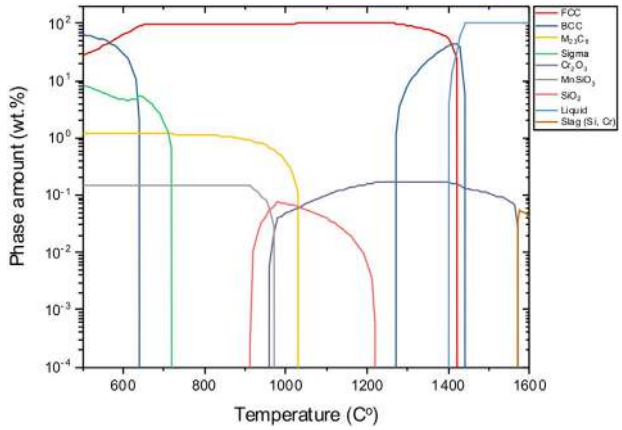

Fig. 4 – Phase fraction as a function of temperature in 316L SS fabricated by SLM: thermodynamic calculations using FactSage software.

We used the thermochemical software FactSage 7.1 [75] with a thermodynamic database (FSstel and FToxid) to calculate the temperature-dependent variations in the equilibrium-phase fraction for the given alloy chemical compositions. As shown in Fig. 4, a stable FCC matrix phase was observed until a temperature of 1410 °C was reached. A metal carbide precipitate, $M_{23}C_6$, was formed at temperatures lower than 500 °C, but it had dissolved when a temperature of 1020 °C was reached. Several oxide phases were present across the entire range of temperatures. Cr_2O_3 became stable at a temperature of 950 °C or higher, whereas $MnSiO_3$ was favored to a temperature of 970 °C. The SiO_2 was thermodynamically stable at temperatures ranging from 910–1220 °C. Fig. 5 shows the back-scattered electron (BSE), ND-IPF, IQ, and KAM maps of as-fabricated SLM specimens. MPBs are marked with black dashed lines to facilitate a comparison of the shapes of the melt pools. The fraction of MPBs observed in the SLM-I specimen was relatively low compared with that observed in the SLM-II specimen. The averages for the width and depth of the melt pools in the SLM-I specimen were 101.1 and 59.17 μm, respectively. The average sizes of the widths and depths of the melt pools in the SLM-II specimen were 101.0 and 52.21 μm, respectively, which indicates that the melt pools in the SLM-I specimen were deeper. That result seemed to be due to the high energy density in the SLM-I specimen. Fig. 5(b) and (f) correspond to the ND-IPF maps of the SLM-I and SLM-II specimens, respectively. The results of the ND-IPF maps indicate that the two as-fabricated specimens did not exhibit the preferred orientation along with the ND. The results are likely due to the influence of process parameters, such as gas flow direction, scanning direction, and layer thickness of fabricated specimens [66,76]. The ND-IPF maps contain columnar grains that appear to track the predominant heat-flow path that resulted from the deposition of follow-on layers. The columnar grains were developed without interference from the MPBs. Fig. 5(c) and (g) show the low-angle grain boundaries (LAGBs), high-angle grain boundaries (HAGBs), and MPBs on the IPF map, which simultaneously developed in the as-fabricated SLM-I and SLM-II specimens. The blue lines represent LAGBs with misorientation angles that ranged from 3°–15°, and the red lines represent HAGBs with misorientation angles ranging from 15°–65°. These results indicate that the columnar grains of the as-fabricated SLM specimens contained relatively high fractions of LAGBs. The KAM distribution in the as-fabricated SLM specimens was not negligible, as shown in Fig. 5(d) and (h). A relatively high KAM was developed in the region of the columnar grains. This result seems related to the thermal contraction induced by the rapid cooling rate during the SLM process.

3.2. *Tensile properties and work hardening rate*

Fig. 6 shows the evolutions of the strain distribution of the miniature specimens, as measured by DIC under uniaxial

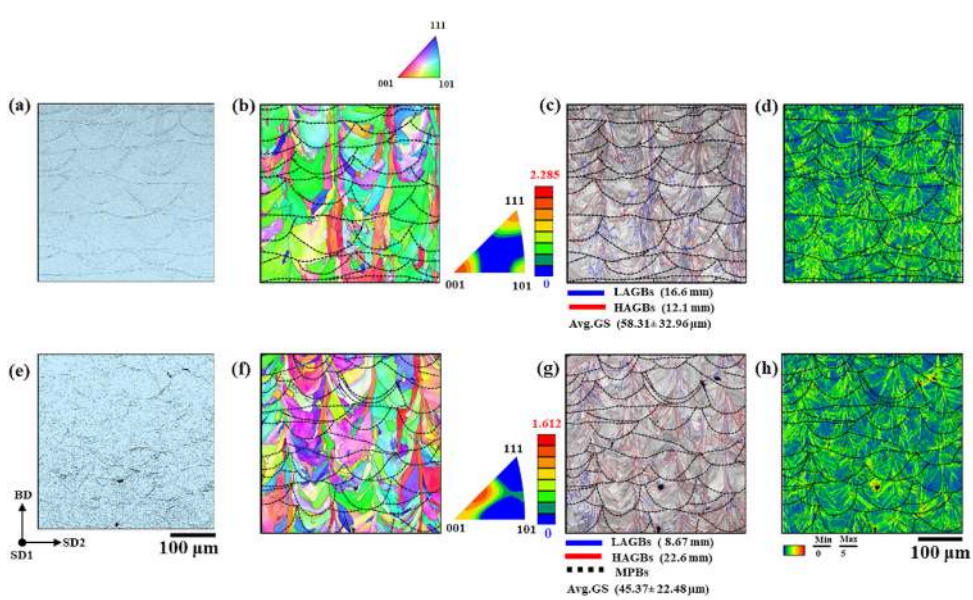

Fig. 5 – EBSD results for the as-fabricated SLM specimens: BSE (a and e), ND-IPF (b and f), IQ (c and g) and KAM (d and h) maps for SLM-I (a, b, c, and d) and SLM-II (e, f, g, and h) specimens. The dotted lines show the presence of the melt pool boundaries in the SLM specimens.

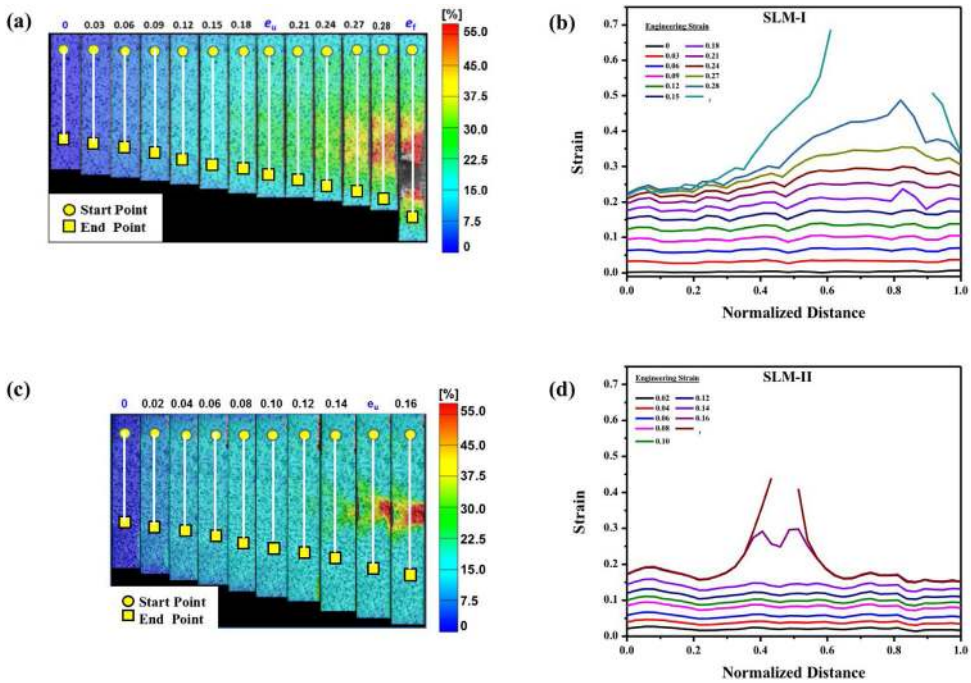

Fig. 6 – Evolutions of the strain distributions of the miniature specimens measured by DIC during uniaxial tension: (a) SLM-I and (c) SLM-II specimens. Line profiles of the strain distribution on the deformed specimens along the LD: (b) SLM-I and (d) SLM-II specimens.

tension. The 2-D strain maps were constructed by utilizing the digital images captured at different stages of the tensile testing using ARAMIS software [73], as shown in Fig. 6(a) and (c). The line profiles of the strain distribution on the deformed specimens along the LD are shown in Fig. 6(b). The SLM-I specimen showed relatively uniform strain distributions until the appearance of a strain of approximately 0.2. Diffuse necking occurred from a strain of 0.2 to a strain of 0.27. The SLM-I specimen exhibited distinctly localized deformation from a strain of 0.28. At an external strain level of 0–0.14, the SLM-II specimen showed a uniform strain, which almost equaled the external strain that occurred along with the LD. In this specimen, localized deformation occurred in a limited region of the specimen with no diffuse necking. Fig. 7(a) and (b) show the representative engineering stress–strain curves of the SLM-I and SLM-II specimens, respectively, obtained from uniaxial tensile tests. Mechanical properties such as yield strength (YS), ultimate tensile strength (UTS), uniform elongation (e_u), and fracture strain (e_f) measured from the engineering stress–strain curve are shown in Table 2. Three experiments were performed for each SLM condition to obtain an average value. Table 2 shows that the YS values for the specimens were similar. Although the SLM-II specimen had a relatively fine grain size compared with that of the SLM-I, as shown in Fig. 5(c) and (g), the relatively high fraction of initial pores in the SLM-II seemed to contribute to a similar level of YS in both specimens. Relatively high levels of scanning speed and laser power contributed to the relatively fine microstructure observed in the SLM-II specimen. The ductility of the SLM-II specimen was lower than that of the SLM-I specimen. This could be related to the relatively low density of the SLM-II specimen. Porosity significantly affects the ductility of 316L SS fabricated by SLM [77]. Fig. 7(c) and (d) show the instantaneous work-hardening rates, ($d\sigma/d\varepsilon$), obtained from the true stress–strain curves of the SLM specimens. The $d\sigma/d\varepsilon$ was rapidly decreased with increases in strain in the early stages of plastic deformation (Region-I). In addition to Region-I, there was a range of strain where the $d\sigma/d\varepsilon$ was decreased in a linear fashion (Region-II). In Regions I and II, since $d\sigma/d\varepsilon > \sigma$ was satisfied, plastic deformation was expected to occur in the absence of necking. Along with Region-II, there was a strain range in Region-III where the $d\sigma/d\varepsilon$ was rapidly decreased again before the $d\sigma/d\varepsilon$ reached either zero or lower, values. The SLM-I region with $d\sigma/d\varepsilon < \sigma$, deformation was expected to become uneven due to the occurrence of necking, as shown in Fig. 6(a). The $d\sigma/d\varepsilon$ decreased sharply in the SLM-II specimen before uniform elongation even though $d\sigma/d\varepsilon > \sigma$. On the other hand, $d\sigma/d\varepsilon = \sigma$ (Considére's criterion) resulted in a fracture that followed a low additional strain before the $d\sigma/d\varepsilon$ had reached 0. As a result, the SLM-I specimen showed a relatively higher level of post-uniform elongation compared with that of the SLM-II specimen. That result seemed to be due to the relatively high fraction of pores in the SLM-II specimen rapidly enhancing the stress triaxiality in the local region after reaching uniform elongation.

3.3. *Effect of microstructure on deformation and fractography*

Fig. 8 shows the BSE and ND-IPF maps of the SLM-I specimen deformed to different levels of strain. The IPF map shows how the spread of orientation gradually increased inside the

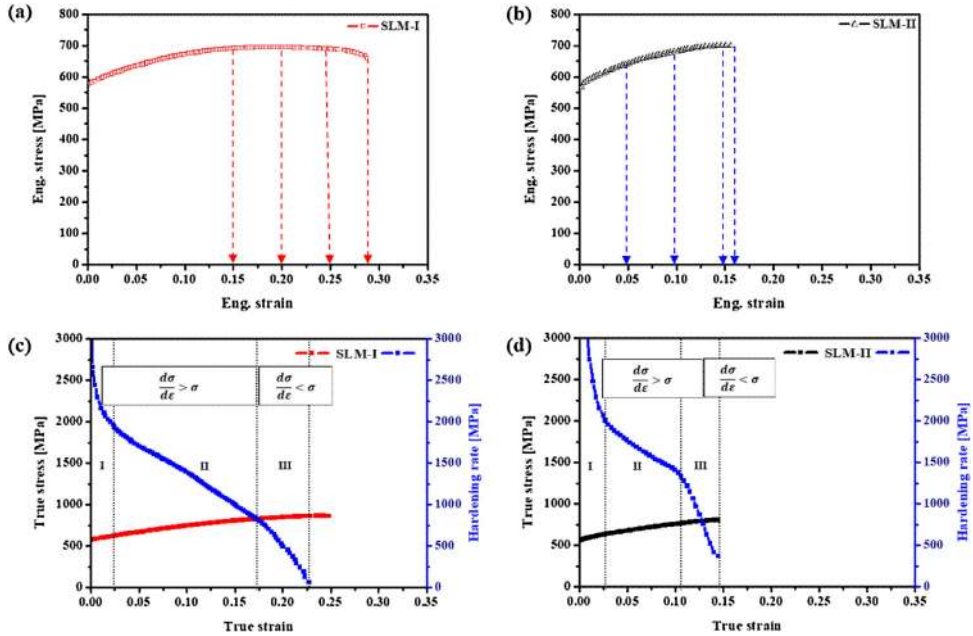

Fig. 7 – Engineering stress–strain curves: (a) SLM-I and (b) SLM-II specimens. True stress–strain and instantaneous work-hardening rate: (c) SLM-I and (d) SLM-II specimens.

Table 2 – Mechanical properties of the SLM specimens.

Specimens	YS [MPa]	UTS [MPa]	e_u	e_f
SLM-I	571 ± 5.7	698 ± 1.8	0.188 ± 0.02	0.29 ± 0.01
SLM-II	551 ± 4.7	705 ± 7.2	0.145 ± 0.01	0.16 ± 0.04

deformed grains as the strain increased. Fig. 8 also shows the development of the IQ, KAM, and Taylor factor (TF) maps for the SLM-I specimen at different levels of strain under uniaxial tension. TF was calculated using the Taylor model based on the assumption that all grains undergo the same strain as the external strain [78]. The distributions of the LAGBs, HAGBs, and Σ3 twin boundaries (TBs) of the deformed specimens appear in the IQ maps. The blue, red, and green lines indicate LAGBs, HAGBs, and Σ3 TBs, respectively. Fig. 9 shows the BSE, ND-IPF, and IQ maps of the SLM-II specimen deformed to different strain levels. In order to differentiate the deformation behavior of the SLM-I specimen described in Fig. 8, the deformation behavior of the SLM-II specimen was analyzed in a region where pores were clustered. The BSE image was used to identify the MPBs in the deformed SLM-II under uniaxial tension. To distinguish the LAGBs from the HAGBs, the MPBs are indicated by the dashed lines in the IPF and IQ maps. The results of the IPF map of the SLM-II specimen under uniaxial tension showed no apparent spreading of the orientation within the deformed grains. The LAGBs and Σ3 TBs in the IQ map of the SLM-II specimen tended to have values lower than those of the SLM-I specimen, as shown in Fig. 8.

Fig. 10(a) shows the results of the quantitative analysis of the boundaries that are developed in the SLM-I specimen under uniaxial tension. The lengths of the LAGBs and HAGBs in the SLM-I specimen increased as the level of strain increased. Fig. 10(b) shows the quantitative results from an analysis of the boundaries developed in the SLM-II specimen under uniaxial tension. The length of the LAGBs and HAGBs in the SLM-II specimen showed no significant change until the strain reached 0.15, but did expose a rapid increase in the e_f. Fig. 10(c) and (d) shows the overall distribution of KAM that developed in both SLM specimens under uniaxial tension. The magnitude of the KAM in both SLM specimens gradually increased as the level of strain increased. A comparison between Fig. 10(c) and (d) show similar levels for the overall distribution of KAM in both the SLM I and SLM II specimens at a strain level of 0.15. To understand the fracture mechanism of the SLM-I specimen, FE-SEM analysis was conducted on the TD section at different levels of strain under uniaxial tension. As shown in Fig. 11, the cracks in the SLM-I specimen before reaching the e_f were observed mainly in the second-phase particles (b, e, f, and i), and some of them were observed in the partially melted powders (h) with weak bonding force. The region (e) where the second-phase particles fell off was also observed. The insets of Fig. 11(f) and (h) list the results of the EDS analyses performed on the second-phase particles and partially melted powders marked in Fig. 11(f) and (h). The EDS analysis explains the possible types of oxide. The thermodynamic calculation given in Fig. 4 shows that several oxides such as Cr_2O_3, $MnSiO_3$, and SiO_2 could form. This calculation result suggests that such oxides could exist as a mixture of several oxides even though their temperature region for thermodynamic stability differs.

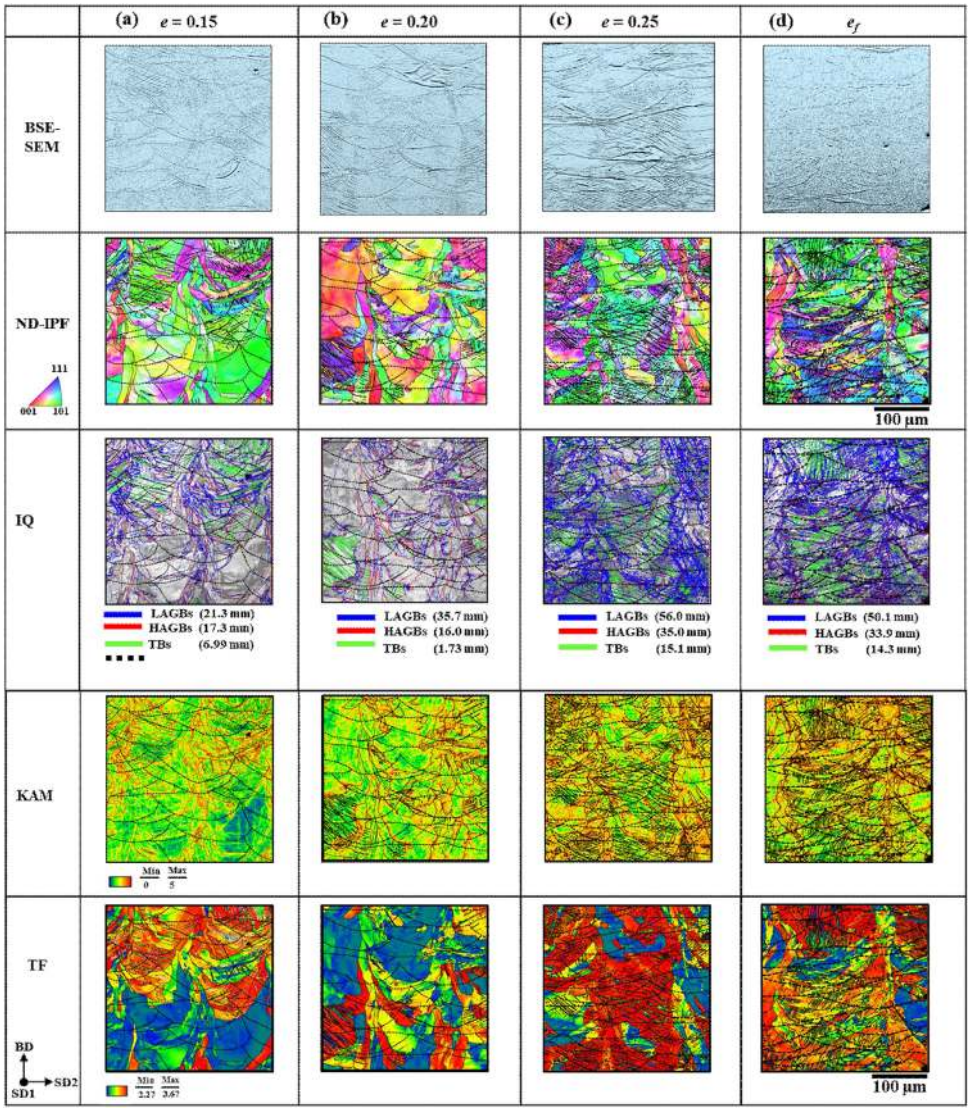

Fig. 8 – BSE, ND-IPF, IQ, KAM and TF maps of the SLM-I specimens deformed to different strain levels: (a) $e = 0.15$, (b) $e = 0.20$, (c) $e = 0.25$, and (d) e_f.

The cross-sectional SEM image at the center region of the SLM-I specimen deformed by fracture strain appears in Fig. 11(j). No evident voids appear in the enlarged SEM images of the insets (k and l) near the fracture surface. Fig. 12 shows the fractography results for the SLM-I specimen following uniaxial tension. The fracture surface of the SLM-I specimen appeared to be a mixture of brittle and ductile modes, as shown in Fig. 12(a) and (b). The type of cleavage on the surface indicates brittle fractures (Fig. 12(a1)). The region of brittle fracture in the SLM-I specimen seems related to the presence of second-phase particles, which favors the propagation of microcracks, as shown in Fig. 12 (a2 and a3). Nano-sized spherical inclusions, indicated by a red arrow, seemed to be generated in the material during the SLM process due to the reaction between the active metals and the oxygen in the protecting chamber [79]. The dimpled surface indicates a ductile mode of fracture, as shown in Fig. 12(b1–b3). The dimpled surface contained micro-voids with less than 1 μm in diameter, which are indicated by the arrow in Fig. 12(b3). The micro-voids seemed to originate mainly from nano-sized inclusions [79]. Fig. 13 features a cross-sectional view of the TD section measured at the center region of the SLM-II specimen and shows the deformation caused by the fracture strain. Comparing Fig. 11(j) and 13(j), cross-section SEM images show that the fractured surface of the SLM-II specimen was relatively rough compared with that of the SLM-I specimen. Here, the roughness of the surface is not a quantitative measurement, but is a just comparison of the cross-section SEM images. As shown in the picture enlarged in Fig. 13, this tendency is considered to be the result of existing pores that are expanded and propagated (c, e and i) along the MPBs. Similar to the SLM-I specimen, cracks in the second-phase particles (b and f), cracks in the partially melted powders (h), and cracks extending from the fracture surface to the cellular structure (l) were also observed. Distinct voids were not observed in the enlarged SEM images shown in the insets of Fig. 13(k) near the fracture surface. The

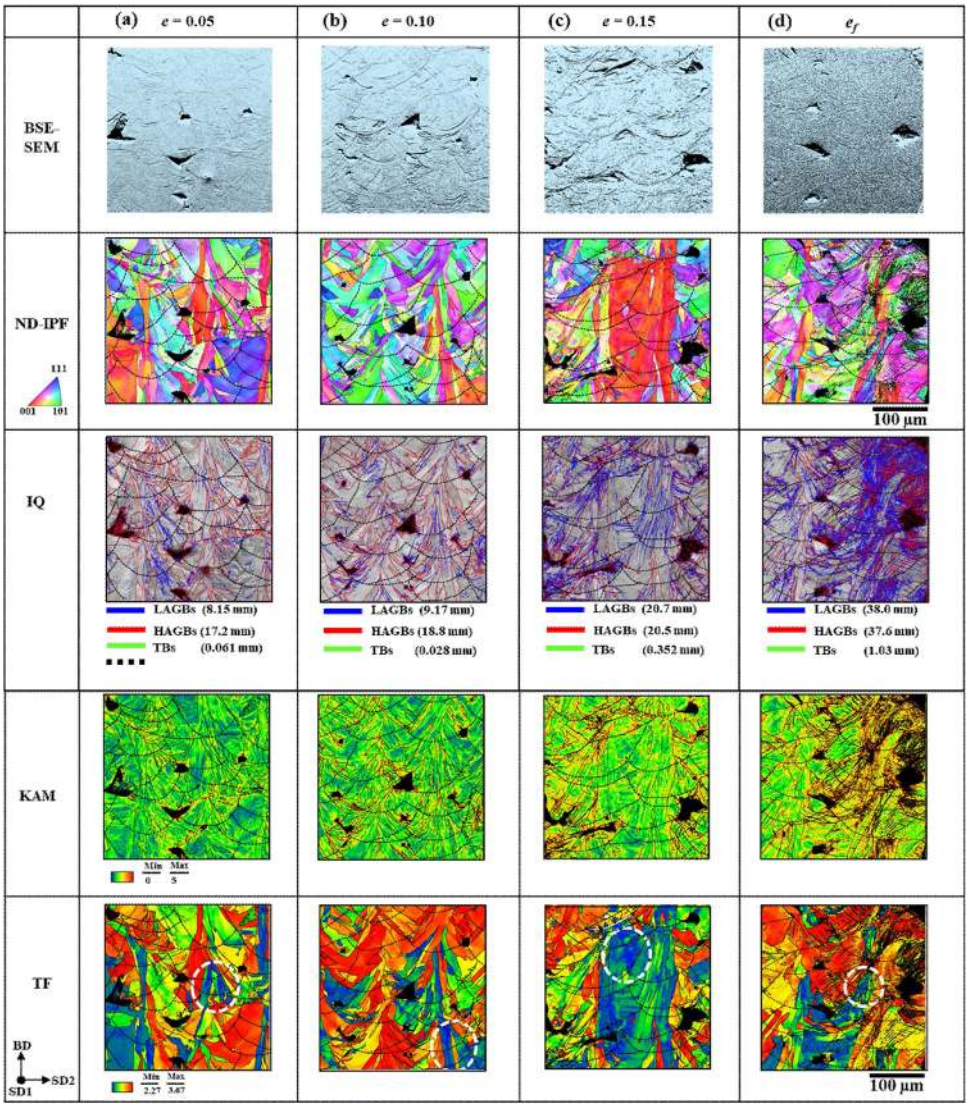

Fig. 9 – BSE, ND-IPF, IQ, KAM and TF maps of the SLM-II specimens deformed to different strain levels: (a) $e = 0.05$, (b) $e = 0.10$, (c) $e = 0.15$, and (d) e_f.

propagation of cracks in the region took place along the MPBs, as shown in Fig. 13(l).

Fig. 14 shows the results of the fractography of the SLM-II specimen following uniaxial tension. Fractures in the surface of the SLM-II also contained a mixture of brittle and ductile modes, as shown in Fig. 14(a) and (b). As shown, the SLM-II specimen had several deep grooves with a similar interval on the fractured surface. These grooves were the result of cracks propagating from the initial pores, as explained in Fig. 3(e). The magnified image of the inner side of the groove shows partially melted powders located in the center of a dimple. These results provided microstructural evidence that clarified why the SLM-II had a relatively low elongation relative to the SLM-I specimen under uniaxial tension. The inset of Fig. 14(c) shows the EDS point analysis, which performed at the locations marked in Fig. 14(a2). The EDS analysis confirmed the presence of the partially melted powders inside the dimples.

4. Discussions

The present study investigated the difference in deformation heterogeneities in SLM-I and SLM-II specimens that were fabricated with energy density values of 83.34 and 66.67 J/mm^3, respectively. This study focused mainly on experimental observations using SEM and EBSD techniques for the purpose of understanding the effect of microstructural factors on the deformation heterogeneities developed in the two as-fabricated SLM specimens under uniaxial tension. Microstructural factors known to develop in as-fabricated SLM specimens can be classified into segregated elements, dislocations, precipitates (or particles), cellular walls, GBs, TBs, crystallographic orientation, MPBs, and pores in the order of size [40,61,79–82].

Wang et al. [44] reported that Cr and Mo tended to segregate in the cellular walls developed on 316L SLM specimens. The sizes of the cellular structures developed in the two as-

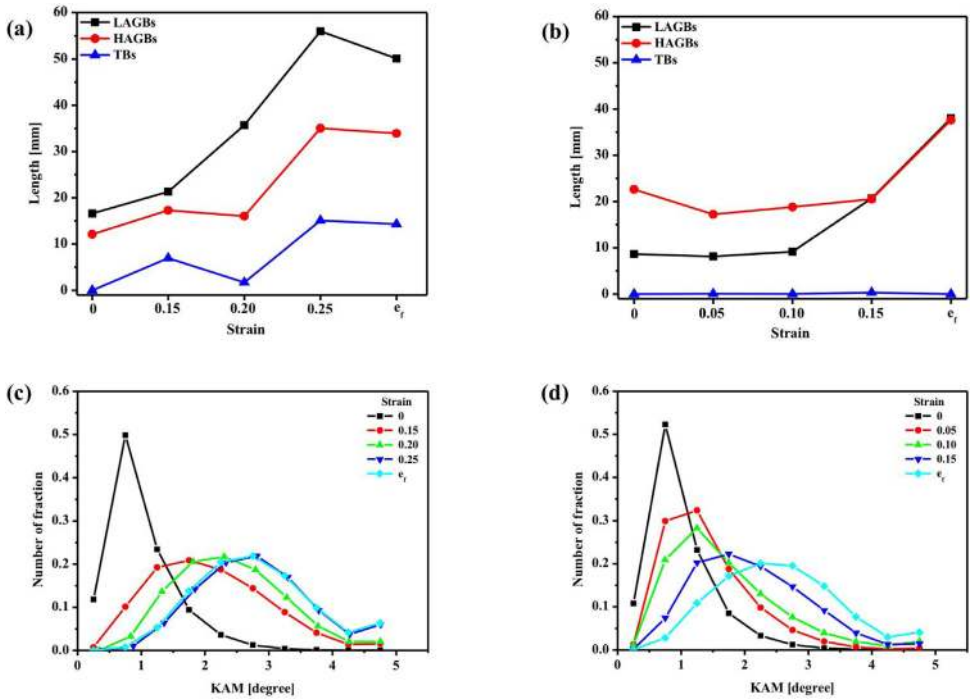

Fig. 10 – Quantitative analysis of boundaries and KAM developed in the SLM specimens during uniaxial tension: (a) and (c) for SLM-I, (b) and (d) for SLM-II.

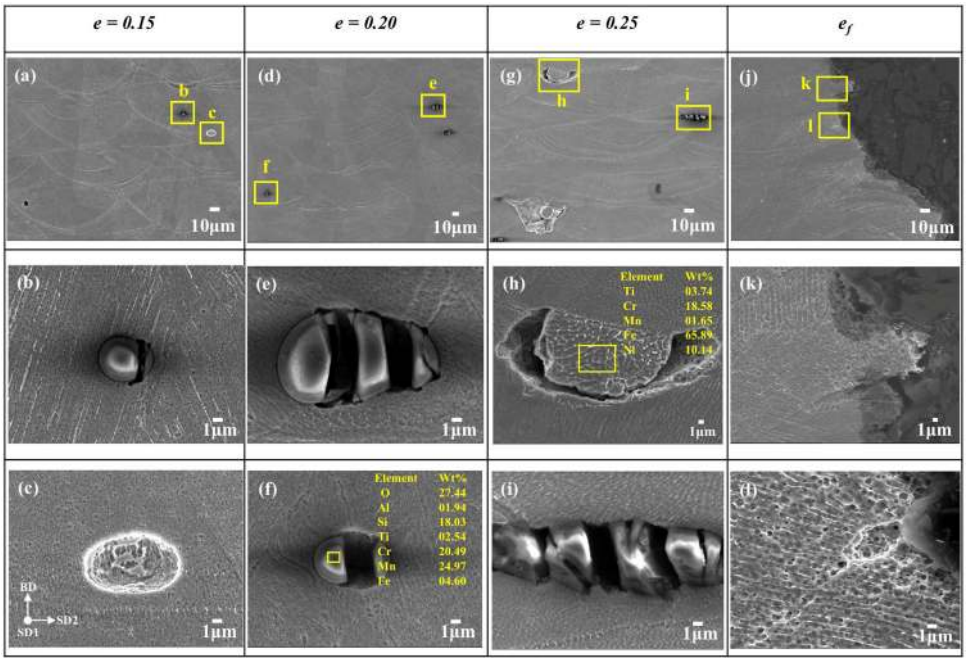

Fig. 11 – FE-SEM images of the SLM-I specimen deformed to different strain levels: (a–c) $e = 0.15$, (d–f) $e = 0.20$, (g–i) $e = 0.25$, and (j–l) e_f.

fabricated SLM specimens shown in Fig. 3(d) and (g) are similar to each other. The distribution of segregated elements that were not covered in this paper can also be expected to have no significant differences in the two as-fabricated SLM specimens. Fig. 10(c) and (d) show that the distribution of KAM developed in the two as-fabricated SLM specimens is very similar. Since the KAM values are proportional to the degree of deformation, the similarity of KAM values indicates that the dislocation densities of the two as-fabricated SLM specimens have similar values. The number fraction of low KAM values (less than 1°) is the highest in the undeformed specimens, while higher KAM values are more pronounced in the deformed specimens. By comparing Fig. 10a and b, it is shown that the SLM-II specimen had a higher fraction of HAGB com-

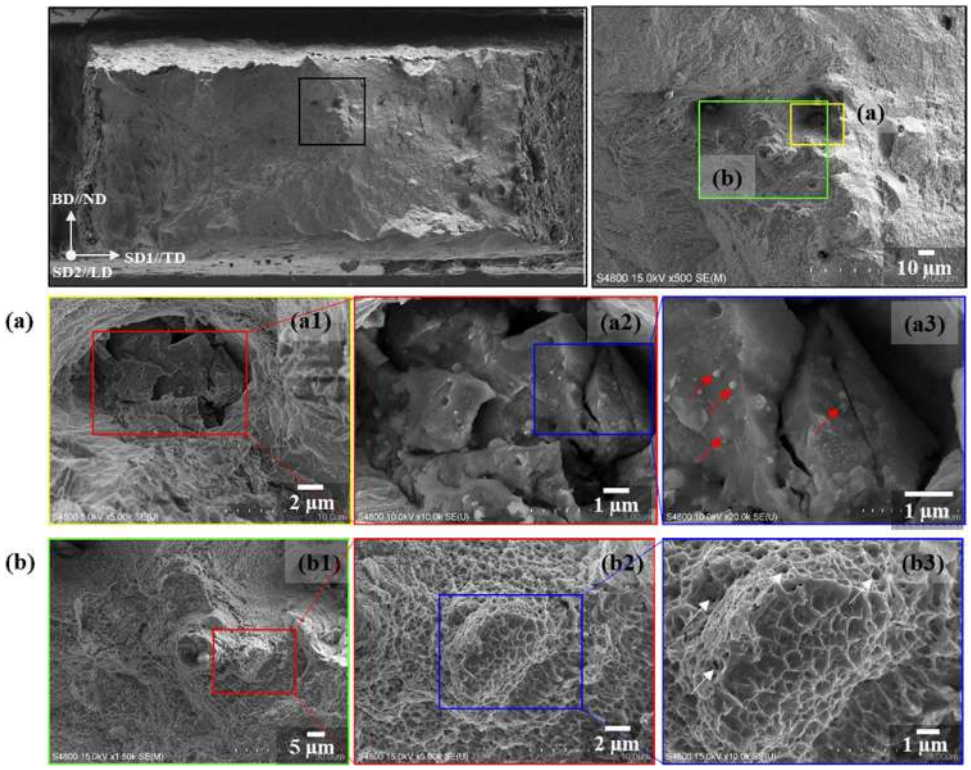

Fig. 12 – Fractography for the SLM-I specimen after uniaxial tensile. FE-SEM images showing the presence of (a1–a3) partially, (b1–b3) completely melted regions.

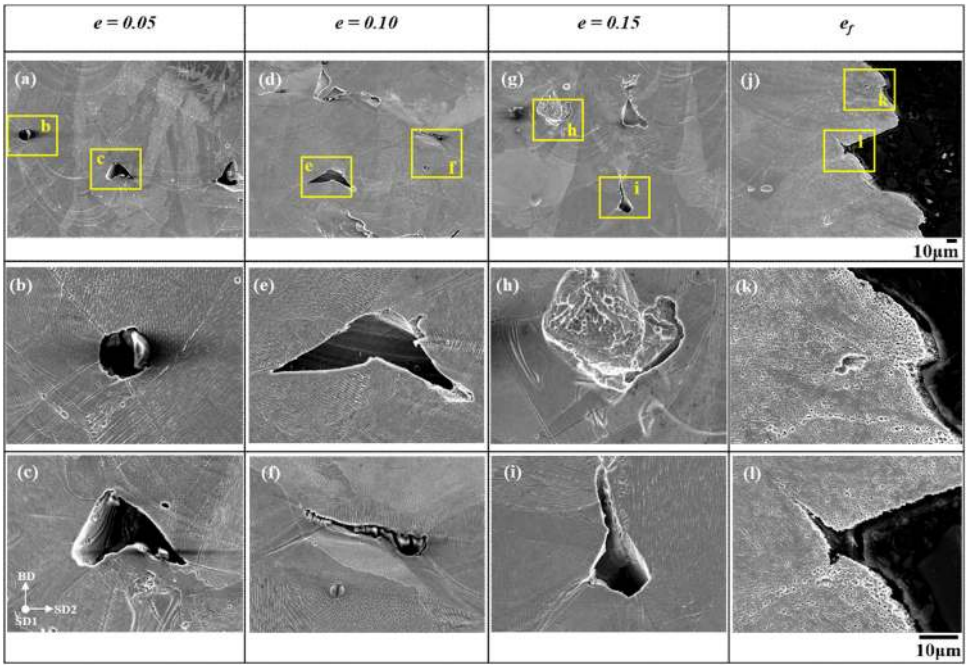

Fig. 13 – FE-SEM images of the SLM-II specimen deformed to different strain levels: (a–c) $e = 0.05$, (d–f) $e = 0.10$, (g–i) $e = 0.15$, and (j–l) e_f.

pared with that of the SLM-I specimen regardless of the level of strain. This result seems to have been due to the difference in energy density imposed into the two specimens during the SLM process. For a more precise explanation, it is necessary to understand the evolutions of the cellular structure that occur after the transformation from liquid to solid state within the MPBs. The effect of HAGBs on deformation heterogeneities in SLM I specimens under uniaxial tensile is capably illustrated

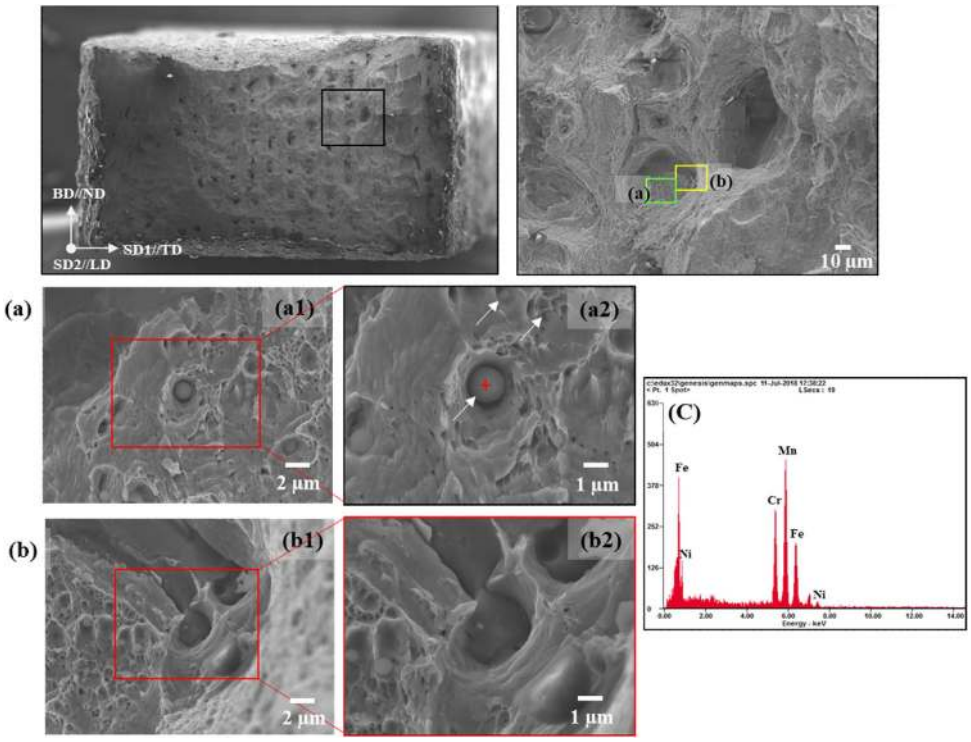

Fig. 14 – Fractography for the SLM-II specimen after the uniaxial tensile. FE-SEM images showing the presence of (a1–a2) partially, (b1–b3) completely melted regions, and (c) EDS analysis indicates the presence of partially melted powder in the grooves.

in Fig. 8. Although the development of Σ3 TBs was also found in some deformed grains, the length of Σ3 TBs in the deformed specimens was not significantly increased under uniaxial tension. Melt pools were elongated with increased strain levels. At strain levels of 0.15 and 0.2, a relatively high KAM value was observed near the HAGBs, while a relatively low level of KAM was observed near the MPBs. As the level of strain increased, a high KAM developed not only in specific HAGBs but also inside specific grains. No increase in the KAM was observed near the MPBs, even under a relatively high level of strain.

Although the SLM-I and SLM-II specimens did not exhibit a preferred orientation, as shown in Fig. 5, the effect of crystallographic orientation on the deformation heterogeneities was evaluated by TF, which depends on the crystallographic orientation. TF can be used as a measure of how much shear strain on active slip systems is induced by the slip of dislocations inside a grain due to a given macroscopic deformation. In other words, it can be expected that grains with high TF will be more severely deformed at the same tensile strain than grains with low TF. By comparing both KAM and the TF maps, Fig. 8 shows that the KAM and the length of Σ3 TBs were high in deformed grains with a relatively high TF value. As explained by Chakrabarty et al. [83], the development of the misorientation is due to the enhanced dislocation density in deformed grains during plastic deformation. This result indicates that the TF map successfully predicted the preferentially deformed regions in the SLM-I specimen under uniaxial tension. The results indicate that the region with a high density of pores in the SLM-II specimen had a relatively low level of plastic deformation compared with that of the SLM-I specimen under uniaxial tension. The results of the KAM and TF maps developed for the SLM-II specimen at different levels of strain under uniaxial tension appear in Fig. 9. Specimens subjected to strains of 0.05 and 0.1 showed a relatively high value for KAM in the vicinity of the pores, while a relatively low value of KAM was observed in the vicinity of the HAGBs. A strain of 0.15 produced relatively high values for KAM in the vicinity of HAGBs in the regions near the pores. Specimens subjected to e_f had a relatively high value of KAM that extended from the vicinity of the pores to the region between the pores. Comparisons of the KAM and TF maps showed that the correlation between the KAM and the TF was relatively weak compared with the results of the SLM-I specimen, as shown in Fig. 8. However, comparing Figs. 8 and 9 show a clear difference in the spatial distribution of KAM developed in both specimens. The SLM-II specimen shows relatively severe non-uniformity of KAM distribution compared with the SLM-I specimen. Since there is no drastic change in the crystallographic orientation in the MPBs, as shown in Fig. 3(c) and (g), a slight difference in the melt pool size seems to have not a significant effect on the deformation heterogeneities of SLM specimens under uniaxial tension.

A large number of pores were formed in the SLM-II specimen. Porosity is a common defect in SLM parts, and it can negatively affect the mechanical properties. Porosity can be classified into two types: gas-induced porosity and process-induced porosity [40,84]. Gas-induced pores with a spherical-shape can occur during gas atomization of 316L SS feedstock prior to the SLM process and may still be present in the final product. On the other hand, the shapes of process-

induced pores are typically non-spherical. Pores form mostly via two situations: (a) where the applied energy is insufficient to completely melt the powder feedstock, which causes a lack of fusion between each adjacent scan and between successive layers; or, (b) where excessive energy absorption induces vaporization or over-melting, which causes large and irregular pores [40,45,85]. The mechanical properties were directly related to the microstructure and defects of the fabricated specimens. The non-uniformity of the KAM distribution implies the presence of deformation heterogeneities and ultimately explains the relatively low ductility of SLM-II, as shown in Fig. 7. The ductility of the SLM-I specimen was better than that of the SLM-II specimens, as shown in Fig. 7a and b. This phenomenon often occurs due to a higher fraction of initial pores. When considering the processing parameters of the SLM-II specimen, the heat input was insufficient to melt the powders due to the high scanning speed. This result indicates that the selection of the proper conditions for laser scanning speed and laser power was crucial in order to minimize the pores in the as-fabricated SLM specimens. The EBSD results explained in Fig. 5 show that the SLM-II specimen (AGS = 45.37 μm) has a finer grain size than the SLM-I specimen (AGS = 58.31 μm). According to the Hall–Petch relationship, the yield strength of the SLM-II specimen should be higher than that of the SLM-I specimen. However, comparing the values of the yield strength measured experimentally in Table 2, the results show the opposite tendency. The reason why the yield strength deviates from the Hall–Petch relationship seems to be that the shape of the grains developed in both SLM specimens is columnar, which greatly deviates from spherical, and the density of the initial pores in both SLM specimens is different. The microstructural factors of the SLM-I specimen seemed to affect the deformation heterogeneities in the following order: crystallographic orientation (or TF) > HAGBs > LAGBs ≈ TBs > MPBs. On the other hand, the microstructural factors of the SLM-II specimen seemed to affect the deformation heterogeneities in the following order: pores > crystallographic orientation (or TF) > HAGBs > LAGBs ≈ TBs > MPBs.

5. Conclusions

Two 316L stainless steel specimens with different microstructures were fabricated with different energy densities of SLM processing. The deformation and fracture behavior under uniaxial tension was analyzed in terms of the main microstructural factors.

1. Uniaxial tensile testing indicated that the SLM-II specimen had a relatively low uniform elongation and fracture strain compared with that of the SLM-I specimen.
2. A relatively high density of pores affected the low level of uniform elongation and the failure strain of the SLM-II specimen.
3. In the SLM-I specimen, as the strain increased, the regions with high KAM values extended to the inside of the deformed grains. In the deformed grains with relatively high TF values, the KAM, or the fraction of Σ3 TBs, was high.
4. In the SLM-II specimen, as the level of strain increased, regions with high KAM values extended from the vicinity of the pores to the regions between the pores.
5. The major microstructural factors affecting deformation heterogeneities in the SLM-I and SLM-II specimens were analyzed to be the crystallographic orientation (or TF values) and the pores, respectively.
6. Analysis of the cross-section of the fractured SLM-I specimen showed that most of the cracks were located in the oxide particles, which was related to the cleavage of the fracture surface.
7. A fractography analysis of the fracture surface revealed that ductile and brittle fracture modes occurred simultaneously in both the SLM-I and SLM-II specimens.

Conflicts of interest

The authors declare no conflicts of interest.

Acknowledgment

This work was supported by the Technology Innovation Program (N0002598) funded by the Ministry of Trade, Industry & Energy (MOTIE, Korea) and Korea Institute for Advancement of Technology.

REFERENCES

[1] Marnier G, Keller C, Noudem J, Hug E. Functional properties of a spark plasma sintered ultrafine-grained 316L steel. Mater Des 2014;63:633–40, http://dx.doi.org/10.1016/j.matdes.2014.06.053.
[2] Keller C, Tabalaiev K, Marnier G, Noudem J, Sauvage X, Hug E. Influence of spark plasma sintering conditions on the sintering and functional properties of an ultra-fine grained 316L stainless steel obtained from ball-milled powder. Mater Sci Eng A 2016;665:125–34, http://dx.doi.org/10.1016/j.msea.2016.04.039.
[3] Mohammadi Zahrani E, Saatchi A, Alfantazi A. Pitting of 316L stainless steel in flare piping of a petrochemical plant. Eng Fail Anal 2010;17:810–7, http://dx.doi.org/10.1016/j.engfailanal.2009.10.015.
[4] Anghelina FV, Ungureanu DN, Bratu V, Popescu IN, Rusanescu CO. Fine structure analysis of biocompatible ceramic materials based hydroxyapatite and metallic biomaterials 316L. Appl Surf Sci 2013;285:65–71, http://dx.doi.org/10.1016/j.apsusc.2013.06.102.
[5] Amanov A, Lee S, Pyun Y. Low friction and high strength of 316L stainless steel tubing for biomedical applications. Mater Sci Eng C 2016;71:176–85, http://dx.doi.org/10.1016/j.msec.2016.10.005.
[6] Zhang L, Wang J. Effect of dissolved oxygen content on stress corrosion cracking of a cold worked 316L stainless steel in simulated pressurized water reactor primary water environment. J Nucl Mater 2014;446:15–26, http://dx.doi.org/10.1016/j.jnucmat.2013.11.027.
[7] Chen XH, Lu J, Lu L, Lu K. Tensile properties of a nanocrystalline 316L austenitic stainless steel. Scr Mater 2005;52:1039–44, http://dx.doi.org/10.1016/j.scriptamat.2005.01.023.
[8] Eskandari M, Zarei-Hanzaki A, Abedi HR. An investigation into the room temperature mechanical properties of

nanocrystalline austenitic stainless steels. Mater Des 2013;45:674–81, http://dx.doi.org/10.1016/j.matdes.2012.08.042.
[9] Kurian A, Prasad MS. A comparison of corrosion resistance of stainless steel fabricated with selective laser melting and conventional processing. Int J ChemTech Res 2015;7:2–6.
[10] Kruth J-P, Mercelis P, Vaerenbergh J Van, Froyen L, Rombouts M. Binding mechanisms in selective laser sintering and selective laser melting. Rapid Prototyp J 2005;11:26–36, http://dx.doi.org/10.1108/13552540510573365.
[11] Yasa E, Kruth JP. Microstructural investigation of selective laser melting 316L stainless steel parts exposed to laser re-melting. Proc Eng 2011;19:389–95, http://dx.doi.org/10.1016/j.proeng.2011.11.130.
[12] Kale AB, Kim B-K, Kim D-I, Castle EG, Reece M, Choi S-H. An investigation of the corrosion behavior of 316L stainless steel fabricated by SLM and SPS techniques. Mater Charact 2020:110204, http://dx.doi.org/10.1016/j.matchar.2020.110204.
[13] Li R, Shi Y, Liu J. Effects of processing parameters on the temperature field of selective laser melting metal powder. Powder Metall 2009;48:186–95, http://dx.doi.org/10.1007/s11106-009-9113-z.
[14] Gu D, Hagedorn YC, Meiners W, Meng G, Batista RJS, Wissenbach K, et al. Densification behavior, microstructure evolution, and wear performance of selective laser melting processed commercially pure titanium. Acta Mater 2012;60:3849–60, http://dx.doi.org/10.1016/j.actamat.2012.04.006.
[15] Casati R, Lemke J, Tuissi A, Vedani M. Aging behaviour and mechanical performance of 18-Ni 300 steel processed by selective laser melting. Metals (Basel) 2016;6:218, http://dx.doi.org/10.3390/met6090218.
[16] Mullen L, Stamp RC, Fox P, Jones E, Ngo C, Sutcliffe CJ. Selective laser melting: a unit cell approach for the manufacture of porous, titanium, bone in-growth constructs, suitable for orthopedic applications. II. Randomized structures. J Biomed Mater Res – Part B Appl Biomater 2010;92:178–88, http://dx.doi.org/10.1002/jbm.b.31504.
[17] Sun J, Yang Y, Wang D. Mechanical properties of a Ti6Al4V porous structure produced by selective laser melting. Mater Des 2013;49:545–52, http://dx.doi.org/10.1016/j.matdes.2013.01.038.
[18] Leedy KD, Stubbins JF. Copper alloy-stainless steel bonded laminates for fusion reactor applications: tensile strength and microstructure. Mater Sci Eng A 2001;297:10–8, http://dx.doi.org/10.1016/S0921-5093(00)01273-9.
[19] Wang L, Wei QS, Xue PJ, Shi YS. Fabricate mould insert with conformal cooling channel using selective laser melting. Adv Mater Res 2012;502:67–71, http://dx.doi.org/10.4028/www.scientific.net/AMR.502.67.
[20] Jeng JY, Peng SC, Chou CJ. Metal rapid prototype fabrication using selective laser cladding technology. Int J Adv Manuf Technol 2000;16:681–7, http://dx.doi.org/10.1007/s001700070039.
[21] Storch S, Nellessen D, Schaefer G, Reiter R. Selective laser sintering: qualifying analysis of metal based powder systems for automotive applications. Rapid Prototyp J 2003;9:240–51, http://dx.doi.org/10.1108/13552540310489622.
[22] Childs THC, Hauser C, Badrossamay M. Selective laser sintering (melting) of stainless and tool steel powders: experiments and modelling. Proc Inst Mech Eng Part B J Eng Manuf 2005;219:339–57, http://dx.doi.org/10.1243/095440505X8109.
[23] Cloots M, Kunze K, Uggowitzer PJ, Wegener K. Microstructural characteristics of the nickel-based alloy IN738LC and the cobalt-based alloy Mar-M509 produced by selective laser melting. Mater Sci Eng A 2016;658:68–76, http://dx.doi.org/10.1016/j.msea.2016.01.058.
[24] Rickenbacher L, Etter T, Hövel S, Wegener K. High temperature material properties of IN738LC processed by selective laser melting (SLM) technology. Rapid Prototyp J 2013;19:282–90, http://dx.doi.org/10.1108/11355254131132328.
[25] Bormann T, Schumacher R, Müller B, Mertmann M, Wild M. Tailoring selective laser melting process parameters for NiTi implants. J Mater Eng Perform 2012;21:2519–24, http://dx.doi.org/10.1007/s11665-012-0318-9.
[26] Bormann T, Müller B, Schinhammer M, Kessler A, Thalmann P, De Wild M. Microstructure of selective laser melted nickel-titanium. Mater Charact 2014;94:189–202, http://dx.doi.org/10.1016/j.matchar.2014.05.017.
[27] Cloots M, Uggowitzer PJ, Wegener K. Investigations on the microstructure and crack formation of IN738LC samples processed by selective laser melting using Gaussian and doughnut profiles. Mater Des 2016;89:770–84, http://dx.doi.org/10.1016/j.matdes.2015.10.027.
[28] Kim D-K, Woo W, Hwang J-H, An K, Choi S-H. Stress partitioning behavior of an AlSi10Mg alloy produced by selective laser melting during tensile deformation using in situ neutron diffraction. J Alloys Compd 2016;686:281–6, http://dx.doi.org/10.1016/j.jallcom.2016.06.011.
[29] Almangour B, Grzesiak D, Yang J. Selective laser melting of TiB 2/316L stainless steel composites: the roles of powder preparation and hot isostatic pressing post-treatment. Powder Technol 2017;309:37–48, http://dx.doi.org/10.1016/j.powtec.2016.12.073.
[30] AlMangour B, Grzesiak D, Yang JM. Rapid fabrication of bulk-form TiB2/316L stainless steel nanocomposites with novel reinforcement architecture and improved performance by selective laser melting. J Alloys Compd 2016;96:150–61, http://dx.doi.org/10.1016/j.jallcom.2016.04.156.
[31] AlMangour B, Grzesiak D, Yang JM. Nanocrystalline TiC-reinforced H13 steel matrix nanocomposites fabricated by selective laser melting. Mater Des 2016;96:150–61, http://dx.doi.org/10.1016/j.matdes.2016.02.022.
[32] Suryawanshi J, Prashanth KG, Ramamurty U. Mechanical behavior of selective laser melted 316L stainless steel. Mater Sci Eng A 2017;696:113–21, http://dx.doi.org/10.1016/j.msea.2017.04.058.
[33] DebRoy T, Wei HL, Zuback JS, Mukherjee T, Elmer JW, Milewski JO, et al. Additive manufacturing of metallic components – process, structure and properties. Prog Mater Sci 2018;92:112–224, http://dx.doi.org/10.1016/j.pmatsci.2017.10.001.
[34] Yakout M, Cadamuro A, Elbestawi MA, Veldhuis SC. The selection of process parameters in additive manufacturing for aerospace alloys. Int J Adv Manuf Technol 2017;92:2081–98, http://dx.doi.org/10.1007/s00170-017-0280-7.
[35] Yakout M, Elbestawi MA, Veldhuis SC. A study of thermal expansion coefficients and microstructure during selective laser melting of Invar 36 and stainless steel 316L. Addit Manuf 2018;24:405–18, http://dx.doi.org/10.1016/j.addma.2018.09.035.
[36] Huang M, Zhang Z, Chen P. Effect of selective laser melting process parameters on microstructure and mechanical properties of 316L stainless steel helical micro-diameter spring. Int J Adv Manuf Technol 2019;104:2117–31, http://dx.doi.org/10.1007/s00170-019-03928-3.
[37] Choong YYC, Chua KHG, Wong CH. Investigation on the integral effects of process parameters on properties of selective laser melted stainless steel parts. Proc Int Conf Prog Addit Manuf 2018;2018(May):274–9, http://dx.doi.org/10.25341/D4P88S.
[38] Simmons J, Daeumer M, Azizi A, Schiffres SN. Local thermal conductivity mapping of selective laser melted 316L stainless steel. In: Solid Free Fabr 2018 Proc 29th Annu Int Solid Free Fabr Symp – An Addit Manuf Conf Rev. 2018. p. 1694–707.

[39] Li R, Shi Y, Wang Z, Wang L, Liu J, Jiang W. Densification behavior of gas and water atomized 316L stainless steel powder during selective laser melting. Appl Surf Sci 2010;256:4350–6, http://dx.doi.org/10.1016/j.apsusc.2010.02.030.
[40] Yusuf SM, Chen Y, Boardman R, Yang S, Gao N. Investigation on porosity and microhardness of 316L stainless steel fabricated by selective laser melting; 2017. p. 1–12, http://dx.doi.org/10.3390/met7020064.
[41] Chen W, Yin G, Feng Z, Liao X. Effect of powder feedstock on microstructure and mechanical properties of the 316L stainless steel fabricated by selective laser melting. Metals (Basel) 2018;8, http://dx.doi.org/10.3390/met8090729.
[42] Liverani E, Toschi S, Ceschini L, Fortunato A. Effect of selective laser melting (SLM) process parameters on microstructure and mechanical properties of 316L austenitic stainless steel. J Mater Process Technol 2017;249:255–63, http://dx.doi.org/10.1016/j.jmatprotec.2017.05.042.
[43] Chen W, Voisin T, Zhang Y, Florien JB, Spadaccini CM, McDowell DL, et al. Microscale residual stresses in additively manufactured stainless steel. Nat Commun 2019;10:1–12, http://dx.doi.org/10.1038/s41467-019-12265-8.
[44] Bahl S, Mishra S, Yazar KU, Kola IR, Chatterjee K, Suwas S. Non-equilibrium microstructure, crystallographic texture and morphological texture synergistically result in unusual mechanical properties of 3D printed 316L stainless steel. Addit Manuf 2019;28:65–77, http://dx.doi.org/10.1016/j.addma.2019.04.016.
[45] Choi J-P, Shin G-H, Brochu M, Kim Y-J, Yang S-S, Kim K-T, et al. Densification behavior of 316L stainless steel parts fabricated by selective laser melting by variation in laser energy density. Mater Trans 2016;57:1952–9, http://dx.doi.org/10.2320/matertrans.M2016284.
[46] Jeon JM, Park JM, Yu JH, Kim JG, Seong Y, Park SH, et al. Effects of microstructure and internal defects on mechanical anisotropy and asymmetry of selective laser-melted 316L austenitic stainless steel. Mater Sci Eng A 2019;763:138152, http://dx.doi.org/10.1016/j.msea.2019.138152.
[47] Cherry JA, Davies HM, Mehmood S, Lavery NP, Brown SGR, Sienz J. Investigation into the effect of process parameters on microstructural and physical properties of 316L stainless steel parts by selective laser melting. In: Advanced Sustainable Manufacturing Technologies (ASTUTE). 2014.
[48] Sutton AT, Kriewall CS, Leu MC, Newkirk JW. Powder characterisation techniques and effects of powder characteristics on part properties in powder-bed fusion processes. Virtual Phys Prototyp 2017;12:3–29, http://dx.doi.org/10.1080/17452759.2016.1250605.
[49] Casati R, Lemke J, Vedani M. Microstructure and fracture behavior of 316L austenitic stainless steel produced by selective laser melting. J Mater Sci Technol 2016;32:738–44, http://dx.doi.org/10.1016/j.jmst.2016.06.016.
[50] Sun Z, Tan X, Tor SB, Chua CK. Simultaneously enhanced strength and ductility for 3D-printed stainless steel 316L by selective laser melting. NPG Asia Mater 2018;10:127–36, http://dx.doi.org/10.1038/s41427-018-0018-5.
[51] Prashanth KG, Scudino S, Eckert J. Defining the tensile properties of Al-12Si parts produced by selective laser melting. Acta Mater 2017;126:25–35, http://dx.doi.org/10.1016/j.actamat.2016.12.044.
[52] Hao L, Dadbakhsh S, Seaman O, Felstead M. Selective laser melting of a stainless steel and hydroxyapatite composite for load-bearing implant development. J Mater Process Technol 2009;209:5793–801, http://dx.doi.org/10.1016/j.jmatprotec.2009.06.012.
[53] Miranda G, Faria S, Bartolomeu F, Pinto E, Madeira S, Mateus A, et al. Predictive models for physical and mechanical properties of 316L stainless steel produced by selective laser melting. Mater Sci Eng A 2016;657:43–56, http://dx.doi.org/10.1016/j.msea.2016.01.028.
[54] Kurzynowski T, Gruber K, Stopyra W, Chlebus E. Correlation between process parameters, microstructure and properties of 316L stainless steel processed by selective laser melting. Mater Sci Eng A 2018;718:64–73, http://dx.doi.org/10.1016/j.msea.2018.01.103.
[55] Zhang B, Dembinski L, Coddet C. The study of the laser parameters and environment variables effect on mechanical properties of high compact parts elaborated by selective laser melting 316L powder. Mater Sci Eng A 2013;584:21–31, http://dx.doi.org/10.1016/j.msea.2013.06.055.
[56] Li P, Wang Z, Petrinic N, Siviour CR. Deformation behaviour of stainless steel microlattice structures by selective laser melting. Mater Sci Eng A 2014;614:116–21, http://dx.doi.org/10.1016/j.msea.2014.07.015.
[57] Yan C, Hao L, Hussein A, Young P, Raymont D. Advanced lightweight 316L stainless steel cellular lattice structures fabricated via selective laser melting. Mater Des 2014;55:533–41, http://dx.doi.org/10.1016/j.matdes.2013.10.027.
[58] Zhang M, Sun C-N, Zhang X, Goh PC, Wei J, David Hardacre HL. Fatigue and fracture behaviour of laser powder bed fusion stainless steel 316L: influence of processing parameters. Mater Sci Eng A 2017;703:251–61, http://dx.doi.org/10.1016/j.msea.2017.07.071.
[59] Riemer A, Leuders S, Thöne M, Richard HA, Tröster T, Niendorf T. On the fatigue crack growth behavior in 316L stainless steel manufactured by selective laser melting. Eng Fract Mech 2014;120:15–25, http://dx.doi.org/10.1016/j.engfracmech.2014.03.008.
[60] Spierings AB, Starr TL, Wegener K. Fatigue performance of additive manufactured metallic parts. Rapid Prototyp J 2013;19:88–94, http://dx.doi.org/10.1108/13552541311302932.
[61] Morris Wang Y, Voisin T, McKeown JT. Additively manufactured hierarchical stainless steels with high strength and ductility. Nat Mater 2017;17:63–71, http://dx.doi.org/10.1038/nmat5021.
[62] Ahmadi A, Mirzaeifar R, Moghaddam NS, Turabi AS, Karaca HE, Elahinia M. Effect of manufacturing parameters on mechanical properties of 316L stainless steel parts fabricated by selective laser melting: a computational framework. Mater Des 2016;112:328–38, http://dx.doi.org/10.1016/j.matdes.2016.09.043.
[63] Kok Y, Tan XP, Wang P, Nai MLS, Loh NH, Liu E, et al. Anisotropy and heterogeneity of microstructure and mechanical properties in metal additive manufacturing: a critical review. Mater Des 2018;139:565–86, http://dx.doi.org/10.1016/j.matdes.2017.11.021.
[64] Thijs L, Verhaeghe F, Craeghs T, Humbeeck J Van, Kruth JP. A study of the microstructural evolution during selective laser melting of Ti-6Al-4V. Acta Mater 2010;58:3303–12, http://dx.doi.org/10.1016/j.actamat.2010.02.004.
[65] Yakout M, Elbestawi MA, Veldhuis SC. Density and mechanical properties in selective laser melting of Invar 36 and stainless steel 316L. J Mater Process Technol 2019;266:397–420, http://dx.doi.org/10.1016/j.jmatprotec.2018.11.006.
[66] Kamath C, El-dasher B, Gallegos GF, King WE, Sisto A. Density of additively-manufactured, 316L SS parts using laser powder-bed fusion at powers up to 400 W. Int J Adv Manuf Technol 2014;74:65–78, http://dx.doi.org/10.1007/s00170-014-5954-9.
[67] Kim DK, Woo W, Kim EY, Choi SH. Microstructure and mechanical characteristics of multi-layered materials composed of 316L stainless steel and ferritic steel produced by direct energy deposition. J Alloys Compd

2019;774:896–907,
http://dx.doi.org/10.1016/j.jallcom.2018.09.390.
[68] Kumar K, Pooleery A, Madhusoodanan K, Singh RN, Chakravartty JK, Dutta BK, et al. Use of miniature tensile specimen for measurement of mechanical properties. Proc Eng 2014;86:899–909,
http://dx.doi.org/10.1016/j.proeng.2014.11.112.
[69] Jahanzeb N, Shin JH, Singh J, Heo YU, Choi SH. Effect of microstructure on the hardness heterogeneity of dissimilar metal joints between 316L stainless steel and SS400 steel. Mater Sci Eng A 2017;700:338–50,
http://dx.doi.org/10.1016/j.msea.2017.06.002.
[70] Mo K, Lovicu G, Chen X, Tung HM, Hansen JB, Stubbins JF. Mechanism of plastic deformation of a Ni-based superalloy for VHTR applications. J Nucl Mater 2013;441:695–703,
http://dx.doi.org/10.1016/j.jnucmat.2013.03.083.
[71] Kale AB, Bag A, Hwang JH, Castle EG, Reece MJ, Choi SH. The deformation and fracture behaviors of 316L stainless steels fabricated by spark plasma sintering technique under uniaxial tension. Mater Sci Eng A 2017;707:362–72,
http://dx.doi.org/10.1016/j.msea.2017.09.058.
[72] Pickerd V. Optimisation and validation of the ARAMIS digital image correlation system for use in large-scale high-strain-rate events; 2013. p. 1–32.
[73] Ls-dyna. Aramis GOM precise industrial 3D metrology changing products; 2015.
[74] Wu Y, San C, Chang C, Lin H, Marwan R. Numerical modeling of melt-pool behavior in selective laser melting with random powder distribution and experimental validation. J Mater Process Technol 2018;254:72–8,
http://dx.doi.org/10.1016/j.jmatprotec.2017.11.032.
[75] Bale CW, Bélisle E, Chartrand P, Decterov SA, Eriksson G, Gheribi AE, et al. Reprint of: FactSage thermochemical software and databases, 2010–2016. Calphad Comput Coupling Phase Diagrams Thermochem 2016;55:1–19,
http://dx.doi.org/10.1016/j.calphad.2016.07.004.
[76] Andreau O, Koutiri I, Peyre P, Penot JD, Saintier N, Pessard E, et al. Texture control of 316L parts by modulation of the melt pool morphology in selective laser melting. J Mater Process Technol 2019;264:21–31,
http://dx.doi.org/10.1016/j.jmatprotec.2018.08.049.
[77] Carlton HD, Haboub A, Gallegos GF, Parkinson DY, MacDowell AA. Damage evolution and failure mechanisms in additively manufactured stainless steel. Mater Sci Eng A 2016;651:406–14,
http://dx.doi.org/10.1016/j.msea.2015.10.073.
[78] Adams BL, Wright SI, Kunze K. Orientation imaging: the emergence of a new microscopy. Metall Trans A 1993;24:819–31, http://dx.doi.org/10.1007/BF02656503.
[79] Zhong Y, Liu L, Wikman S, Cui D, Shen Z. Intragranular cellular segregation network structure strengthening 316L stainless steel prepared by selective laser melting. J Nucl Mater 2016;470:170–8,
http://dx.doi.org/10.1016/j.jnucmat.2015.12.034.
[80] Wang D, Song C, Yang Y, Bai Y. Investigation of crystal growth mechanism during selective laser melting and mechanical property characterization of 316L stainless steel parts. JMADE 2016;100:291–9,
http://dx.doi.org/10.1016/j.matdes.2016.03.111.
[81] Qiu C, Kindi MA, Aladawi AS, Hatmi IA. A comprehensive study on microstructure and tensile behaviour of a selectively laser melted stainless steel. Sci Rep 2018;8,
http://dx.doi.org/10.1038/s41598-018-26136-7.
[82] Saeidi K, Gao X, Zhong Y, Shen ZJ. Hardened austenite steel with columnar sub-grain structure formed by laser melting. Mater Sci Eng A 2015;625:221–9,
http://dx.doi.org/10.1016/j.msea.2014.12.018.
[83] Chakrabarty S, Mishra SK, Pant P. Crystallographic orientation and boundary effects on misorientation development in austenitic stainless steel. Mater Sci Eng A 2014;617:228–34,
http://dx.doi.org/10.1016/j.msea.2014.08.058.
[84] Sames WJ, List FA, Pannala S, Dehoff RR, Babu SS. The metallurgy and processing science of metal additive manufacturing. Int Mater Rev 2016;61:315–60,
http://dx.doi.org/10.1080/09506608.2015.1116649.
[85] Gong H, Rafi K, Gu H, Starr T, Stucker B. Analysis of defect generation in Ti–6Al–4V parts made using powder bed fusion additive manufacturing processes. Addit Manuf 2014;1–4:87–98,
http://dx.doi.org/10.1016/j.addma.2014.08.002.